

Supporting Information

Electrode Engineering of Redox-Active Conjugated Microporous Polymers for Ultra-High Areal Capacity Organic Batteries

*Antonio Molina^{aψ}, Nagaraj Patil^{aψ}, Edgar Ventosa^a, Marta Liras^b, Jesus Palma^a, and Rebeca
Marcilla^{a*}*

^aElectrochemical Processes Unit, IMDEA Institute, Avda. Ramón de la Sagra 3, 28935
Móstoles, Spain

^bPhotoactivated Processes Unit, IMDEA Energy, Avda. Ramón de la Sagra 3, 28935 Móstoles,
Spain

^ψ*Equal contribution of both authors*

AUTHOR INFORMATION

Corresponding Author

*E-mail: rebeca.marcilla@imdea.org

Estimation of materials cost for anthraquinone-based Li-ion stationary battery

The evolution of the materials cost for a Li-ion battery in which inorganic-based cathode is replaced by organic-based one is estimated for the best-case scenario. This means that only the cost of anthraquinone is assumed without additional cost derived from its functionalization. A high utilization rate is also assumed, i.e. 200 mAh g⁻¹. A cell voltage of 2.5 V is used since anthraquinone operated at around this value. The rest of elements, e.g., graphite, separator, current collectors, are the same as in current Li-ion batteries (45 % electrode porosity). The prices used for the calculation are listed in Table S1.

Table S1. List of elements in a graphite–anthraquinone Li-ion battery and their corresponding prices

Material	Cost (USD·kg ⁻¹)	Reference
Anthraquinone	5	¹
Graphite	10	²
Carbon	7.15	²
Non-aqueous electrolyte	19.5	²
Material	Cost (USD·m ²)	Reference
Non-aqueous positive current collector	0.3	²
Non-aqueous negative current collector	1.2	²
Separator	2.7	²

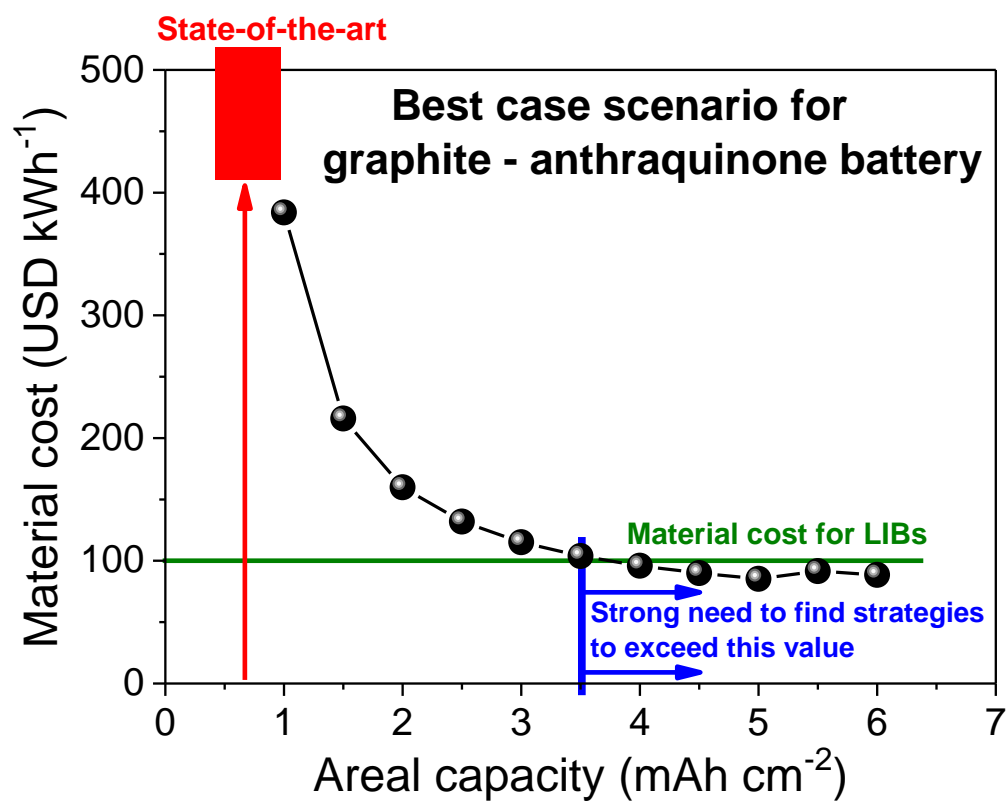


Figure S1. Evolution of battery cost for graphite – anthraquinone Li-ion battery with the areal capacity.

EXPERIMENTAL SECTION

Materials

Copper (I) iodide (CuI; 98%, Alfa Aesar), 2,6-dibromoanthraquinone (95%, Fluorochem), tetrakis(triphenylphosphine) palladium (0) (Pd(PPh₃)₄; 99%, Sigma Aldrich), 1,3,5-triethynylbenzene (>98%, Alfa Aesar), reduced graphene oxide (RGO; Nanografi), single-walled carbon nanotubes (SWCNT; Nanografi) multi-walled carbon nanotubes (MWCNTs; Elicarb[®] MW, Thomas-Swan), polyvinylidene fluoride (PVDF; Sigma Aldrich), lithium bis(trifluoromethanesulfonyl)imide (LiTFSI; 99%, Fluorochem), triethylamine (Et₃N; 99%, Alfa Aesar), hexadecyltrimethylammonium bromide (CTAB; ≥98%, Sigma Aldrich), 1-methyl-2-pyrrolidinone (NMP; ≥99%, Sigma Aldrich), carbon coated aluminum foil (PI-KEM) and lithium foil (Sigma Aldrich) were used as received. 1,2-dimethoxyethane (DME; 99.5%, Sigma Aldrich), 1,3-dioxolane (DOL; 99.8%, Sigma Aldrich), anhydrous *N,N*-dimethylformamide (DMF; >99.8%, Sigma Aldrich) were dried over 4 Å molecular sieves for at least 48 h, distilled, and stored under argon prior to use. Tetrahydrofuran (THF), toluene, methanol (MeOH), dichloromethane (CH₂Cl₂) were of the highest grade, purchased from Chemlab and used without further purification.

Synthesis of Conjugated Microporous Polymers based on Anthraquinone

Synthesis of IEP-11. Anthraquinone-based conjugated microporous polymer was synthesized by following a two-step pathway combining miniemulsion polymerization method and ulterior solvothermal treatment (12 h) through Sonogashira cross-coupling reaction, as reported in our previous article.³

Synthesis of IEP-11-Xy hybrids materials. Anthraquinone-based conjugated microporous polymer/nanocarbon hybrid materials were synthesized following a similar procedure than for IEP-11-E but with the addition of carbon additive prior to the miniemulsion and solvothermal reaction steps. Nanocarbon additives such as MWCNTs, SWCNTs and reduced carbon oxide (RGO) were used in different percentages. They are abbreviated as **IEP-11-Xy** where **X** stands for M, S or R (for MWCNTs, SWCNTs and RGO, respectively) and **y** stands for 5, 10 or 20 (for different %wt). As a representative example, IEP-11-M20 was synthesized as follows: First, the ultrasonic dispersion of MWCNTs (60 mg) suspensions in Et₃N (7 mL) and toluene (7 mL) solvent mixture was obtained with the aid of probe-type sonicator for 10 min. Then, 2,6-dibromoanthraquinone (0.44 mmol, 161 mg), 1,3,5-triethynylbenzene (0.666 mmol, 100 mg), Pd(PPh₃)₄ (0.017 mmol, 20 mg) and CuI (0.035 mmol, 6 mg) were added to the aforementioned dispersion under stirring. Further, the polymerization process *via* the miniemulsion and solvothermal steps and the purification of the obtained hybrid materials proceeded similar to the synthesis of IEP-11-E. The mass content of carbon additive in the obtained hybrid material was determined based on the gravimetric yield of the reaction. Other hybrid materials, IEP-11-M10, IEP-11-S10 and IEP-11-S5R5 with 10% of MWCNTs, 10% of SWCNTs and 5/5% of SWCNTs/RGO, respectively, were also synthesized as summarized in Table S2. The yields of hybrids materials were determined by gravimetry, and found in the range of 70–80 %.

Physico–chemical Characterization

Fourier-transform infrared spectra (FTIR) were recorder on a Nicolete 6700 from Thermo Scientific and are reported in terms of frequency of absorption (cm⁻¹). ¹³C NMR spectra were recorder with Bruker Avance III/HD 100 MHz spectrometer. Raman spectra were acquired using a JASCO NRS-5100 spectrometer equipped with an exciting laser (532 nm). The microscopic

features of IEP-11-Xy and their composite electrodes were carried out using transmission electron microscopy (TEM; JEOL JEM 2100HT). The TEM images were acquired with 200 kV electron acceleration energy.

The specific surface area and pore-size distribution were determined by N₂ adsorption–desorption isotherms at 77 K analysis and were carried out using Autosorb iQ2-Quantachrome Instruments. Before analysis, the samples were thoroughly dried and degassed at 100 °C for 10 h to remove the adsorbed gases/moisture. The specific surface area was calculated by two methods; Brunauer, Emmett and Teller equation (BET) (S_{BET}) and total pore volume (V_{tot}), micropore volume (V_{micro}) and microporous and mesoporous surface area ($S_{\text{micro/DFT}}$, $S_{\text{meso/DFT}}$) were also determined by Quenched Solid Density Functional Theory (QSDFT) method using a calculation model with slit, cylindrical and sphere pores (S_{DFT}).

Preparation of Electrodes

Slurry-casting method. The electrodes were prepared by mixing the IEP-11-Xy hybrid material with PVDF in NMP (90/10 and 80/20 ratio ($f_{\text{wt}\%}$)) were investigated. In those electrodes the carbon additive is incorporated to the hybrid prior to polymerization and no additional carbon was added during the electrode preparation. The mixing process was carried out with a scatter IKA Ultra-Turrax T10 S with three intervals of 10 min dispersion and 5 min relaxing sequences. The resulting slurry was uniformly slurry-casted onto carbon coated aluminium foil (10 mm diameter), and the electrode was dried overnight at 50 °C under vacuum. Electrodes with low active-material mass loading ($\sim 0.3 \text{ mg cm}^{-2}$) and high active-material mass loading ($\sim 15 \text{ mg cm}^{-2}$) were prepared following this method as indicated in Table S2. As a control experiment, electrode calendering compaction process was applied to selected electrodes. For comparison, composite electrode based on IEP-11 polymer, MWCNTs and PVDF with 70/20/10 ($f_{\text{wt}\%}$)

composition was also prepared. This electrode was named IEP-11@M20 where @ indicates that carbon additive is added during the electrode ink preparation and not prior to polymerization as in the hybrids. The composition and mass loading of all prepared electrodes are included in Table S2.

Buckypaper electrodes. Different from the aforementioned traditional slurry-casting, we also prepare buckypaper composite electrodes with the hybrid IEP-11-S5R5. Following this methodology, SWCNTs was used as binder (and conductive additive) instead of PVDF during the electrode formulation. The use of SWCNTs facilitated the formation of a stable ink and the construction of buckypaper electrodes with very high mass loadings (up to 60 mg cm⁻²). Typically, 45 mg of IEP-11-S5R5 and 5 mg of SWCNTs (90/10 wt%) were added to 10 mL of NMP and the dispersion was sonicated for 1 h in a bath sonicator (Branson 2510, 100 W, 42 kHz). After being stirred for another 2 h at room temperature, a stable ink-like suspension was obtained. The suspension was filtrated through a Nylon filter (pore size ~0.45 µm) with the aid of vacuum, followed by thorough rinsing with NMP to remove loosely bound polymer. The buckypaper was carefully peeled off from the filter and dried overnight at 50 °C under vacuum. The buckypaper electrodes were cut into circular discs with a diameter of 10 mm with mass loading of the active-material in the range of 9–60 mg cm⁻² (the higher amount of suspension filtered the higher the mass loading). In another control experiment, buckypaper electrode based on IEP-11/SWCNTs/RGO with 80/15/5 (*f*_{wt%}) composition and mass loading of 15 mg cm⁻² was also formulated. This electrode was named IEP-11@S15R5 where @ indicates that carbon additives are added during the electrode ink preparation and not prior to polymerization as in the hybrids. The electrode material composition of all the composite electrodes investigated in this work is detailed in Table S2.

Electrochemical Characterization

Electrochemical performance of different cathodes was performed in CR 2032 coin-type cells with a porous Whatman® glass microfiber filter (Grade GF/B) soaked with 200 μL (unless specifically stated otherwise) of electrolyte (1 M LiTFSI in DME/DOL (1:1 v/v)) and using lithium foil as anode. The cells were assembled in a high-purity argon-filled glovebox (MBraun; $\text{H}_2\text{O} < 0.5$ ppm and $\text{O}_2 < 1.5$ ppm) to avoid any possible contamination by oxygen/moisture.

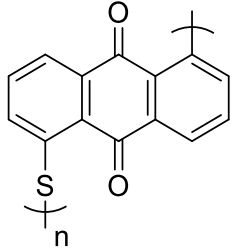
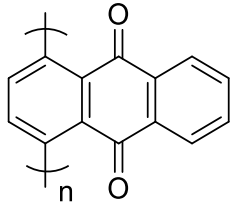
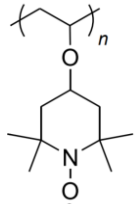
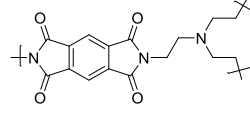
The electrochemical performance of electrodes was investigated by cycling voltammetry and galvanostatic charge–discharge (GCD) using Bio-logic VMP3 multichannel Potentiostat/Galvanostat (Biologic SP-150). The GCD experiments were carried out at different C-rates from 0.03–10 C in the range of 1.5–3.5 V (vs Li/Li⁺). Lower cut-off potential of 1.5 V was chosen since reduction reaction (discharge cycle) occurs at potentials > 1.5 V. Gravimetric capacity of the electrodes and current rates (C-rates) are based on the weight of the active-material (IEP-11 polymer) in the electrode. Areal capacity is calculated based on geometrical area of the electrode (0.785 cm^2).

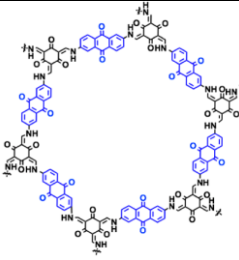
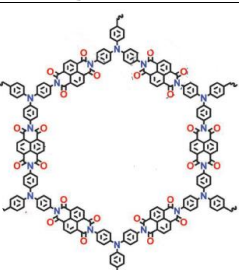
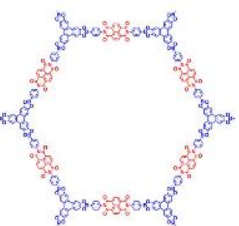
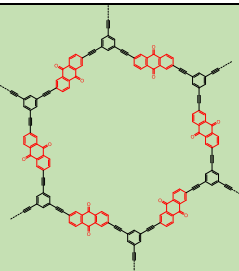
Table S2. Electrode material composition of all the composite electrodes investigated in this work

composite electrode	mass loading ^a	electrode fabrication method	polymer/hybrid material (%)	carbon additive added during the ink preparation (%)	PVDF (%)
IEP-11-M20	~0.3 mg cm ⁻²	slurry-casting ^b	IEP-11-M20 (90)	—	10
IEP-11-M10	~0.3 mg cm ⁻²	slurry-casting ^b	IEP-11-M10 (90)	—	10
IEP-11-S10	~0.3 mg cm ⁻²	slurry-casting ^b	IEP-11-S10 (90)	—	10
IEP-11-S5R5	~0.3 mg cm ⁻²	slurry-casting ^b	IEP-11-S5R5 (90)	—	10
IEP-11@M20	~0.3 mg cm ⁻²	slurry-casting ^b	IEP-11 (70)	MWCNT (20)	10
IEP-11-S5R5	~15 mg cm ⁻²	slurry-casting ^b	IEP-11-S5R5 (90)	—	10
IEP-11-S5R5 ^c	~15 mg cm ⁻²	slurry-casting ^b	IEP-11-S5R5 (90)	—	10
IEP-11-S5R5 ^c	~15 mg cm ⁻²	slurry-casting ^b	IEP-11-S5R5 (80)	—	20
IEP-11-S5R5@S10	~9–60 mg cm ⁻²	buckypaper ^d	IEP-11-S5R5 (90)	SWCNT (10)	—
IEP-11@S15R5	~30 mg cm ⁻²	buckypaper ^d	IEP-11 (80)	SWCNT/RGO (15/5)	—

^aThe loading of hybrid material in the composite electrode determined by gravimetry. ^bElectrode slurry was uniformly slurry-casted onto carbon coated aluminum foil. ^cCalendering compaction process applied to these electrodes. ^dMetal current collector- and binder-free self-standing electrodes obtained *via* vacuum-assisted filtration procedure.

Table S3. State-of-the-art of organic electrodes employed in Li-ion batteries

active-material ^{REF}	mass loading (mg cm ⁻²)	C _g , theo, C _g , max., active-material utilization (%) (mAh g ⁻¹)	cycle performance: C _{g/a} , first/max., C _{g/a} , last, C _{g/a} , retention, number of cycles, speed (C-rate or A g ⁻¹)	rate performance: C _{g/a} , C _{g/a} , retention at different C-rates (or A g ⁻¹)	cell configuration: anode electrolyte cathode active material/ conducting additive/binder, wt/wt/wt%	S _{BET} (m ² g ⁻¹)
Linear Redox-Active Polymers or hybrid thereof						
 PAQS ⁴	n.r.	225 ^a 187 83%	205 ^a 200 97% 10 0.1C	170 ^a , 100%, 0.1C 160, 94%, 0.5C 120, 70%, 50C 60, 35%, 200C	Li 1 M LiTFSI 2 : 1 DOL : DME (v:v) Cathode PAQS 6% CNT/Super P/PTFE 6:3:1	161
 P14AQ ⁵	1.0	260 ^a 257 99%	0.25 ^b 0.24 98% 1000 0.2C 0.5 mA cm ⁻²	0.26, ^b 100%, 0.2C 0.25, 96%, 1C 0.2, 76%, 10C	Li 1 M LiTFSI 2 : 1 DOL : DME (v/v) cathode (P14AQ/KB/PTF E, 6:3:1)	n.r.
 PTVE ⁶	2.2	135 ^a 104 77%	n.r.	0.3, ^b 100%, 1C 0.24, 80%, 5C 0.15, 52%, 30C 0.1, 31%, 80C	Li 1 M LiPF ₆ 3 : 7 EC : DEC (v/v) cathode (PTVE/VGCF/C MC/PTFE, 80:15:4:1)	n.r.
 PMTA/SWCNT ⁷	4.0	383 ^a 179 47%	0.60 ^b 0.51 86.6% 200 0.5C	0.64, ^b 100%, 0.1C 0.56, 88%, 1C 0.44, 69%, 5C 0.28, 44%, 10C	Li 1 M LiTFSI 1:1 DOL : DME (v/v) cathode PMTA-10.9% SWCNT/CC/PTF E 65:30:5	59
Redox-Active Porous Polymers or hybrid thereof						

 DAAQ-ECOF ⁸	0.45	151 ^a 145 96%	0.037 ^b 0.035 94% 1800 0.2 mA cm ⁻²	0.06, ^b 100%, 0.1C 0.047, 74%, 3C 0.03, 50%, 10C	Li 1 M LiTFSI TGEDME cathode (DAAQ-ECOF /super P/PVDF, 6:3:1)	216
 2D-PAI-CNT ⁹	1.2	126 ^a 104 82%	97.1 ^a 97.1 8000	0.124, ^b 100%, 1.6C 0.122, 98%, 3.2C 0.117, 94%, 6.3C 0.116, 93%, 7.9C 0.115, 92%, 16C	Li 1 M LiTFSI 1 : 1 DOL : DME (v/v) cathode (2D-PAI- CNT(5:5) /super P/Alg-Na, 8:1:1)	768
 DTP-ANDI-COF ¹⁰	1.0	82.4 ^a 67 81%	0.066 ^b 0.066 100% 700 2.4 C	0.066, ^b 100%, 2.4C 0.065, 98%, 3.6C 0.061, 92%, 6C 0.059, 88%, 9C 0.057, 86%, 12C	Li 1 M LiTFSI 1 : 1 EC : DMC (v/v) cathode DTP-ANDI- COF/SuperP/PV DF 7:2:1	478
 IEP-11-S5R5 (This work)	0.3–60	149 ^a 149 100%	0.71 ^b 0.44 63% 300 1C *vs Li 0.44 ^b 0.37 83% 1000 1C *vs LFP	6.3, ^b 100%, 0.03C 6.0, 96%, 0.15C 5.4, 87%, 0.5C 4.6, 74%, 1C 3.5, 56%, 2C 2.0, 32%, 5C 0.8, 13%, 10C	Li 1 M LiTFSI 1 : 1 DOL : DME (v/v) IEP-11- S5R5 (IEP-11- S5R5/SWCNT, 9:1)	960

^aGravimetric capacity (C_g) is calculated based on mass of active-material in the cathode and expressed in mAh g⁻¹. ^bAreal capacity (C_a) is calculated based on geometrical area of the electrode and expressed in mAh cm⁻². Theoretical gravimetric capacity ($C_{g, \text{theo}}$) = (26801 x n) / MW; n = number of electrons involved in the redox process, MW = molecular weight of the redox-active repeating units. Material activity = ($C_{g, \text{max.}}$ / $C_{g, \text{theo}}$) x 100. $C_{g/a, \text{initial/last/max.}}$ = initial / last cycle / maximum gravimetric/areal discharge capacity obtained during the cycle performance experiments. Capacity retention = ($C_{g/a, \text{max. or first cycle}}$ / $C_{g/a, \text{last cycle}}$) x 100. nC-rate designates that the current chosen will charge/discharge the battery in 1/n h. n.d. = not determined, n.r. = not reported.

Electrolyte salts: lithium hexafluorophosphate (LiPF₆), lithium bis(trifluoromethanesulfonyl)imide (LiTFSI).

Electrolyte molecular solvents: ethylene carbonate (EC), diethyl carbonate (DEC), dimethyl carbonate (DMC), tetraglyme (TGEDME/G4), 1,3-dioxolane (DOL), 1,2-dimethoxyethane (DME).

Carbon additives: Conductive carbon (CC), acetylene black (AB), carbon black (CB), Ketjen black (KB), carbon nanotubes (CNTs), multi-walled carbon nanotubes (MWCNTs), single-walled carbon nanotubes (SWCNTs), reduce graphene oxide (RGO).

Binders: poly(vinylidenedifluoride) (PVDF), poly(tetrafluoroethylene) (PTFE), sodium alginate (Alg-Na).

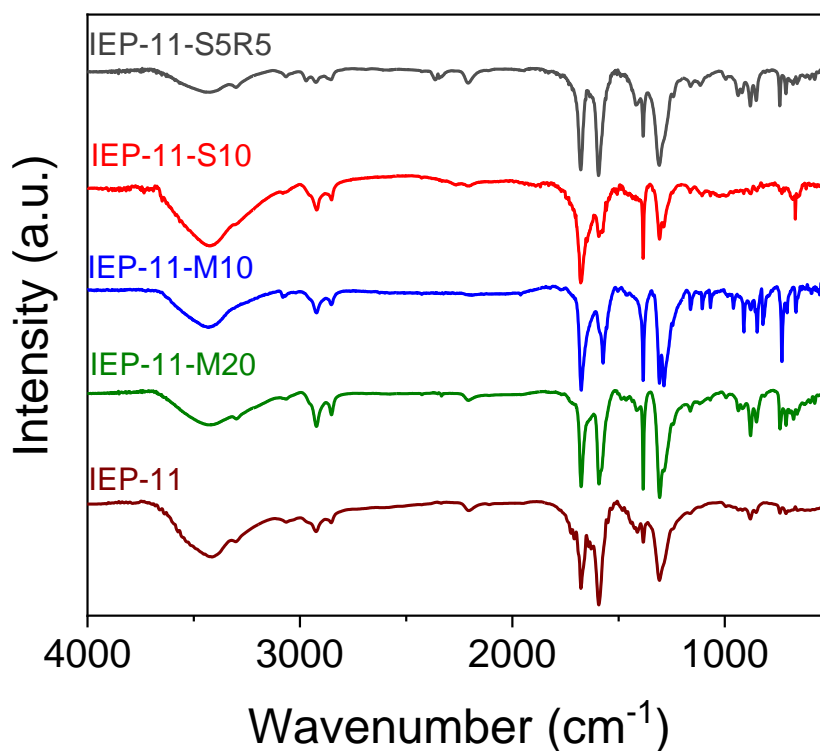


Figure S2. FTIR spectra of IEP-11 polymer and IEP-11-Xy hybrid materials.

Different IEP-11-Xy hybrid materials presented nearly identical spectral characteristics and similar to that of IEP-11 polymer. The presence of characteristic signals at 1670 cm^{-1} and 1600 cm^{-1} corresponding to the stretching vibrations of C=O and C=C, respectively, confirm successful incorporation of anthraquinone units into the polymer matrices in all the IEP-11 and IEP-11-Xy samples.

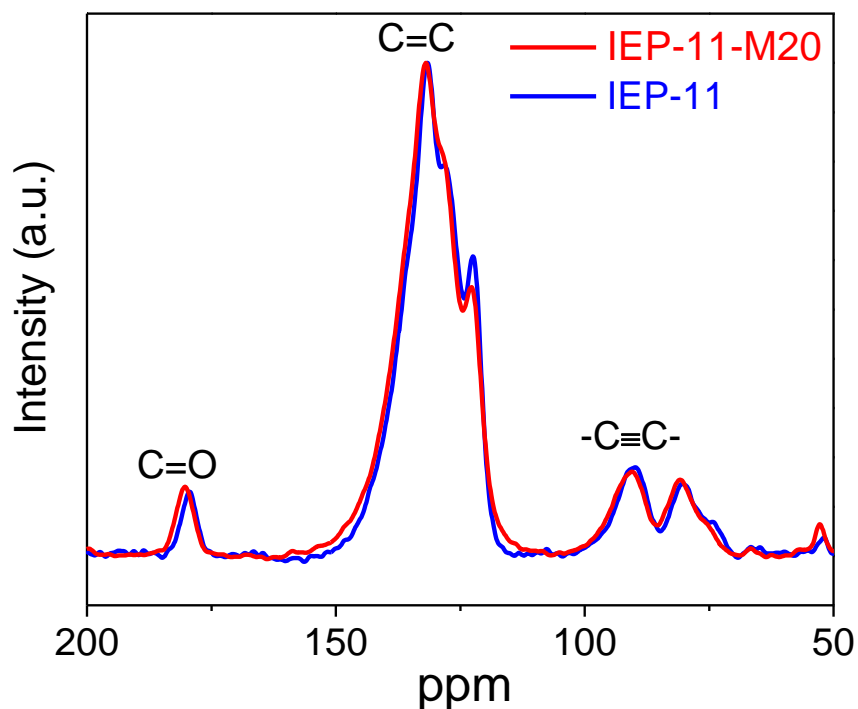


Figure S3. Solid-state ^{13}C NMR spectra of IEP-11 and IEP-11-M20.

The co-existence of three characteristic resonance peaks centered at 180, 130 and 85 ppm corresponding to the C=O (of anthraquinone unit), C=C (of aromatic ring) and $-\text{C}\equiv\text{C}-$ (of linker unit), respectively, once again suggests that both the IEP-11 and IEP-11-Xy samples featured similar chemical composition, irrespective of the addition of MWCNT carbon into the polymer matrices in the case of IEP-11-M20.

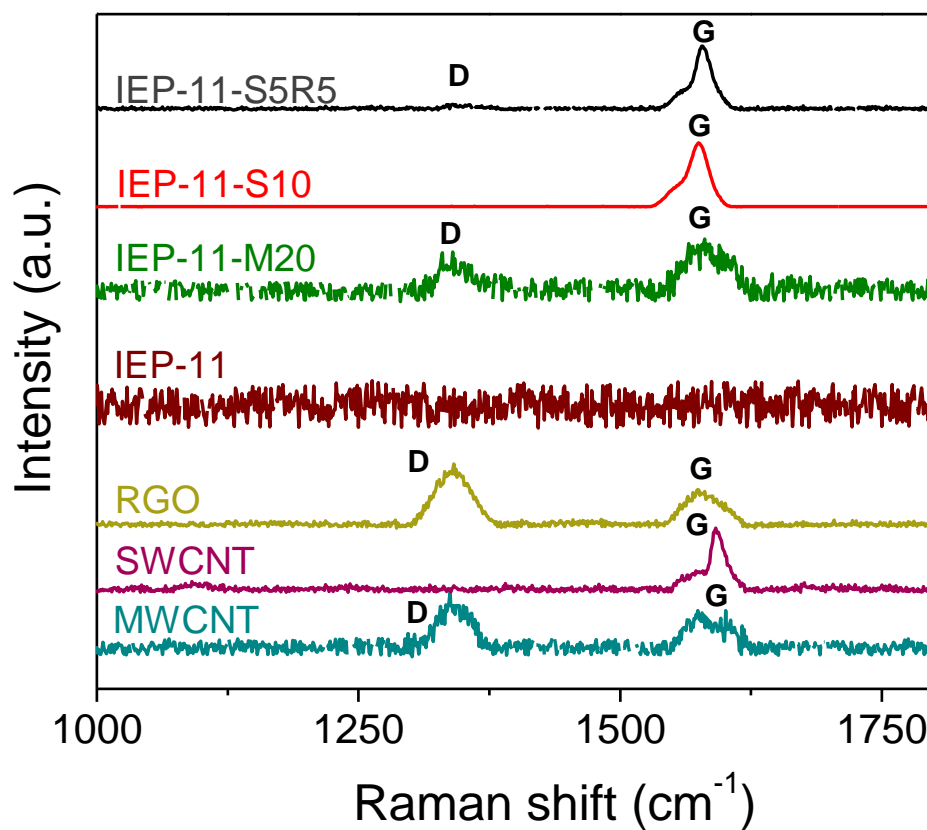


Figure S4. Raman spectra of IEP-11 polymer and IEP-11-Xy hybrid materials.

The Raman spectra of MWCNT and RGO show two prominent peaks at $1343\text{ cm}^{-1}/1581\text{ cm}^{-1}$ and $1340\text{ cm}^{-1}/1578\text{ cm}^{-1}$, respectively, correspond to the D/G bands.^{11,12} The G-band is attributed to the ordered sp^2 carbon lattice, while the D-band is ascribed to the graphene layer defects and disorders. The spectrum of SWCNT shows a prominent peak at 1590 cm^{-1} (G-band) with a shoulder around 1564 cm^{-1} .

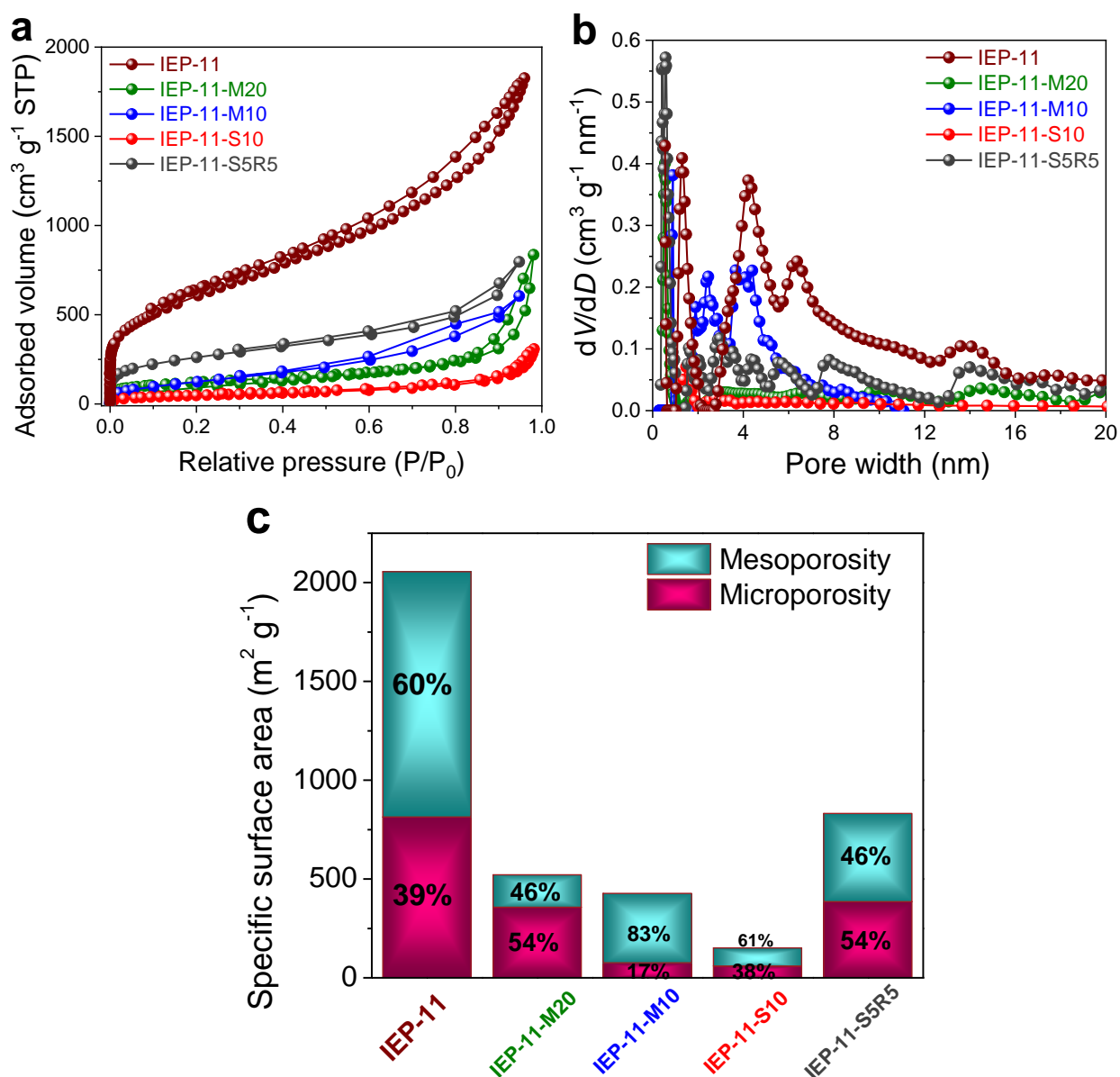


Figure S5. a) Nitrogen adsorption–desorption isotherm profiles, b) pore-size distributions from the QSDFT model, and c) percentages of micro/mesoporosity for IEP-11 polymer and IEP-11-Xy hybrid materials.

Table S4. Textural parameters obtained from N₂ adsorption–desorption isotherms at 77 K

Polymer	$S_{\text{BET}}^{\text{a}}$ (m ² g ⁻¹)	$S_{\text{DFT}}^{\text{b}}$ (m ² g ⁻¹)	$S_{\text{micro/DFT}}^{\text{c}}$ (m ² g ⁻¹)	$S_{\text{meso/DFT}}^{\text{c}}$ (m ² g ⁻¹)	$S_{\text{micro/DFT}}$ (%)	$S_{\text{meso/DFT}}$ (%)	$V_{\text{tot}}^{\text{d}}$ (cm ³ g ⁻¹)	V_{micro} (cm ³ g ⁻¹)	V_{micro} (%)
IEP-11	2200	2075	813	1242	39	60	2.70	0.32	12
IEP-11-M20	437	356	165	191	46	54	0.78	0.09	11
IEP-11-M10	477	426	75	351	17	83	0.8	0.06	7
IEP-11-S10	170	150	58	92	38	61	0.45	0.03	6
IEP-11-S5R5	940	831	384	447	46	54	1.15	0.2	17

^aSpecific surface area calculated using Brunauer-Emmett-Teller method. ^bSpecific surface determined using Quenched Solid Density Functional Theory (QSDFT) method using a calculation model with slit, cylindrical and sphere pores. ^cMicroporous and mesoporous surface area determined using QSDFT method. ^dTotal pore volume and micropore volume (< 2 nm) calculated from QSDFT model.

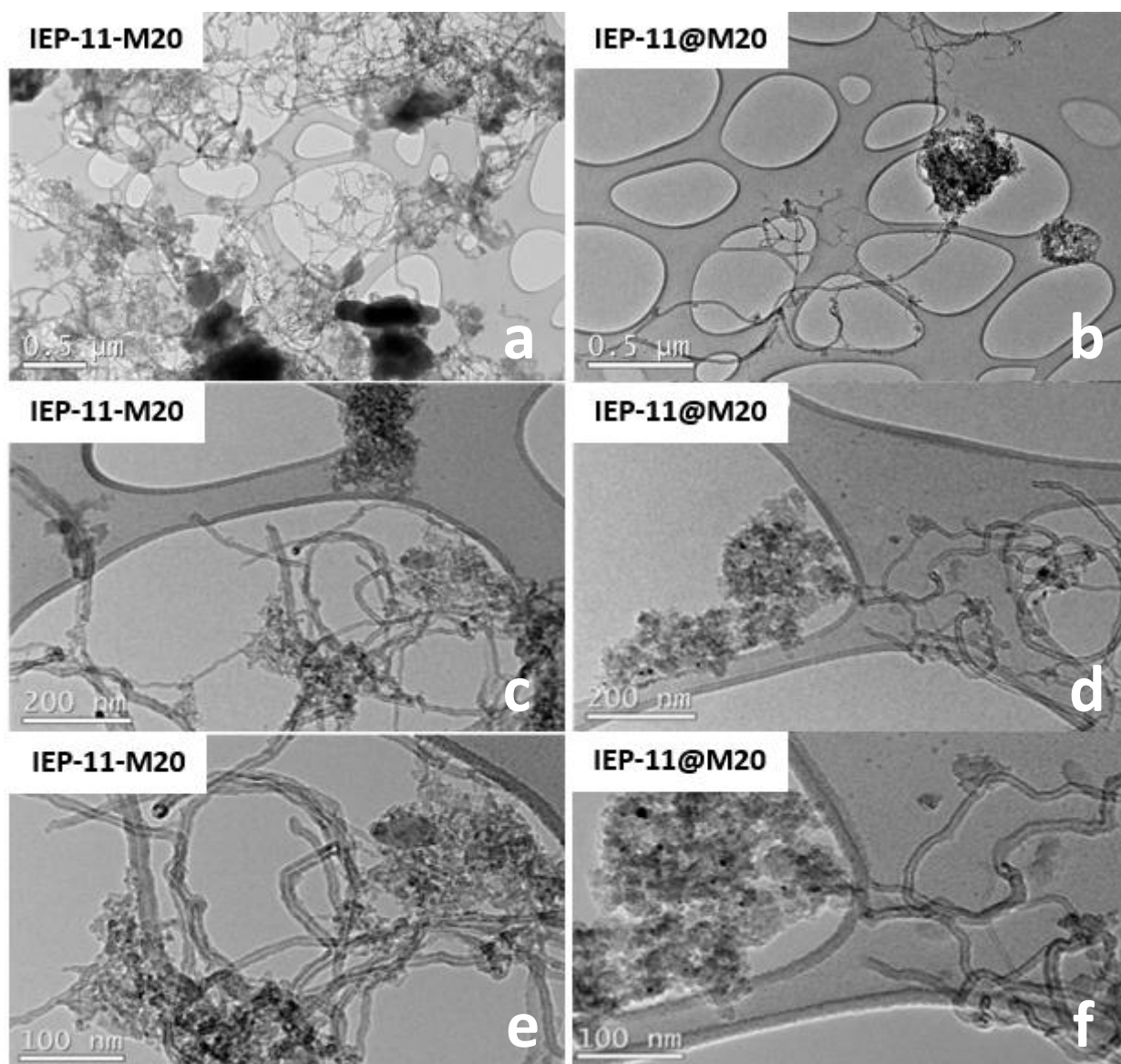


Figure S6. TEM images of IEP-11@M20 and IEP-11-M20 at different magnifications. Scale bar is 500 (Figure S6a, b), 200 (Figure S6c, d), and 100 nm (Figure S6e, f).

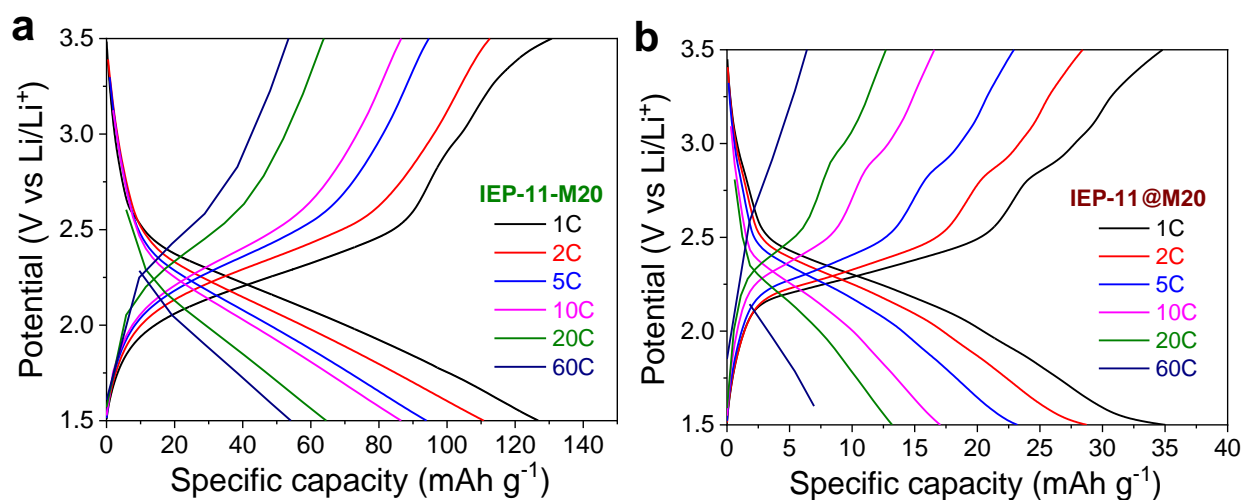


Figure S7. The representative galvanostatic specific capacity–potential profiles obtained at different C-rates in Li-ion half-cells for (a) IEP-11-M20, and (b) IEP-11@M20 electrodes.

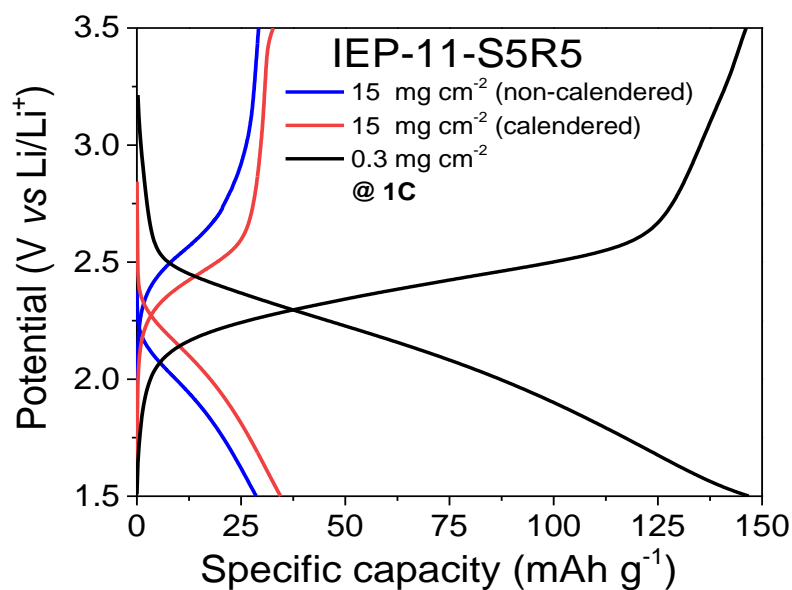


Figure S8. Specific capacity–potential profiles of slurry-casted electrodes, recorded at 1C in Li-ion half-cells. IEP-11-S5R5 high mass loading electrodes with/without calendering process.

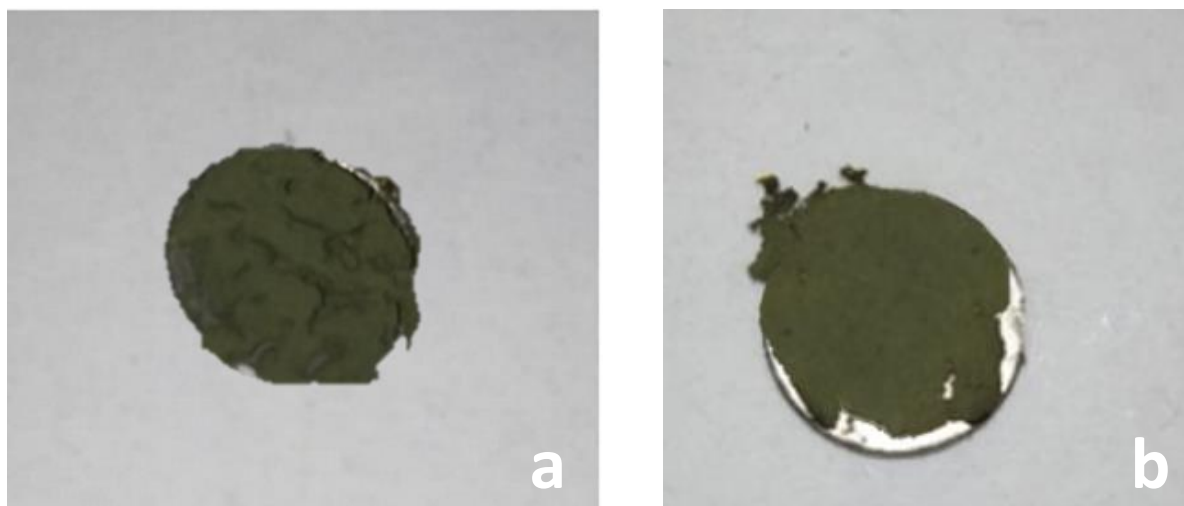


Figure S9. Digital images of high mass loading (15 mg cm^{-2}) IEP-11-S5R5 slurry-casted electrodes onto the carbon-coated aluminum foil. (a) without applying calendaring procedure, and (b) calendered electrode.

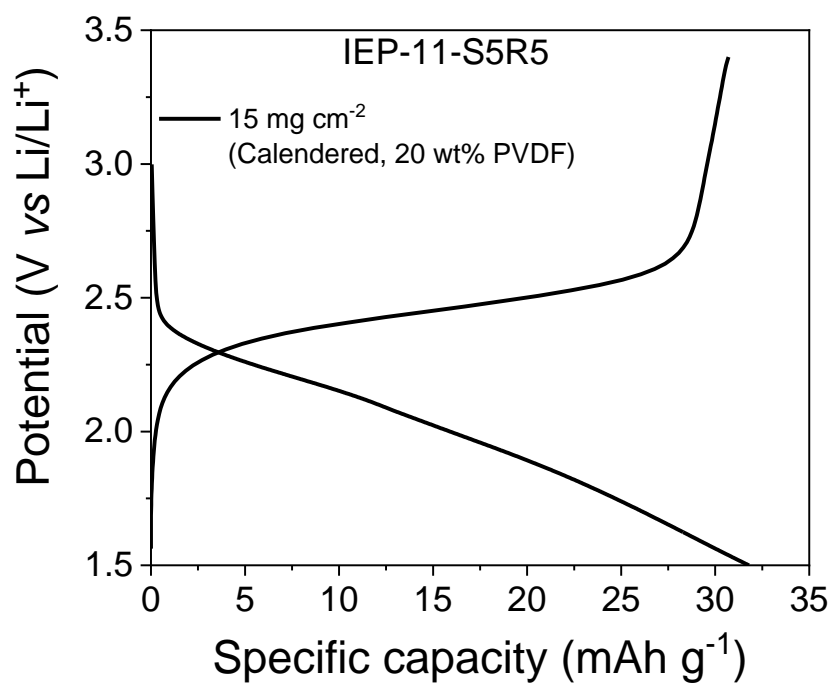


Figure S10. Specific capacity–potential profile of calendered IEP-11-S5R5 electrode with a mass loading of 15 mg cm^{-2} and 20 wt% PVDF binder, recorded at 1C in Li-ion half-cell.

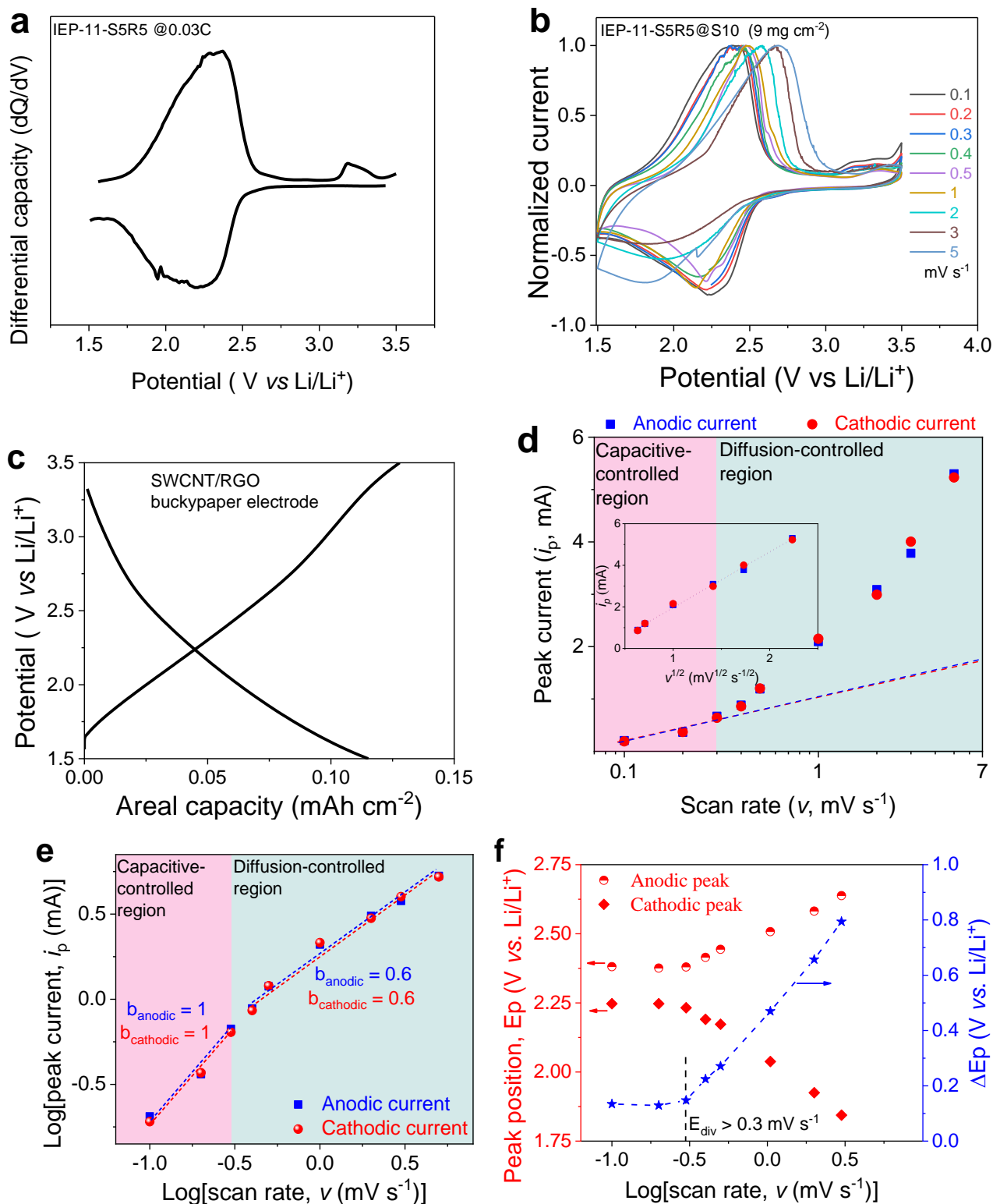


Figure S11. (a) Differential capacity – potential plot for IEP-11-S5R5@S10 (9 mg cm⁻²) at 0.03 C. (b) CVs of IEP-11-S5R5@S10 (9 mg cm⁻²) at different scan rates. The CVs are normalized by the peak anodic current to show the peak shift with the scan rates. (c) GCD profile of buckypaper based on SWCNTs and RGO at 1C. Kinetic analysis of IEP-11-S5R5@S10 (9 mg cm⁻²): (d) Variation of anodic and cathodic peak current as a function of scan rate. Inset display *v*^{1/2}-dependance of the of anodic and cathodic peak current in the diffusion-controlled region. (e) Plot of peak current vs scan rate in logarithmic scale to obtain *b*-values according to *i_p* = *av^b*. (f)

Variation of anodic and cathodic peak positions (E_p), and ΔE_p as a function of the scan rate (in logarithmic scale).

In general, the currents (i) in the CV curves as a function of the scan rate (ν) obeys a power-law relationship as:

$$i = a\nu^b$$

Where, a and b are adjustable coefficients. The exponential b -value can be determined by the slope of $\log(i)$ versus $\log(\nu)$ plot for cathodic and anodic peaks (Figure S11e)

$$\log i = \log a + b \log \nu$$

Ideally, the b -value of 0.5 indicates a semi-infinite linear diffusion-controlled process, whereas the b -value of 1.0 is the signature of a capacitive-controlled behaviour (surface-controlled and/or not limited by the diffusion). When $b = 0.5$, the current response in the voltammogram is proportional to the square root of the scan rate (S11d) as:

$$i = nFACD_{app}^{1/2} \nu^{1/2} \pi^{1/2} \chi(bt) (\alpha nF / RT)^{1/2}$$

where F is the Faraday constant, A is the surface area of the electrode material, C is the Li^+ concentration within the cathode, D_{app} is the apparent diffusion coefficient, the function $\chi(bt)$ represents the normalized current α is the transfer coefficient, n is the number of electrons involved in the electrode reaction, R is the molar gas constant and T is the absolute temperature.

When b takes the value of 1.0, the current is proportional to the scan rate (S11d) as:

$$I = \nu C_d A$$

where C_d is the capacitance (F).

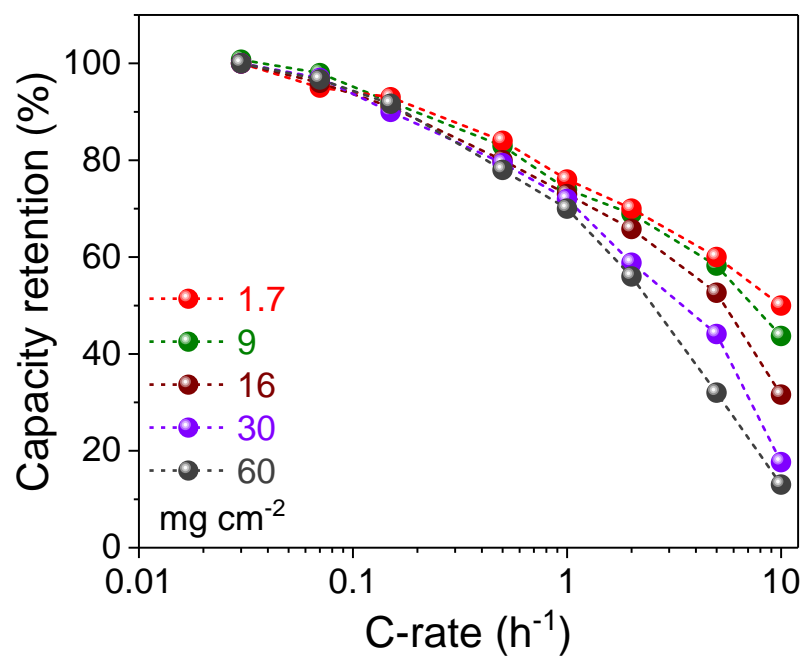


Figure S12. Rate performance (capacity retention rate) of IEP-11-S5R5@S10 buckypaper electrodes with different mass loadings in Li-ion half-cells. The capacities at higher C-rates are normalized with respect to the capacity at 0.03C.

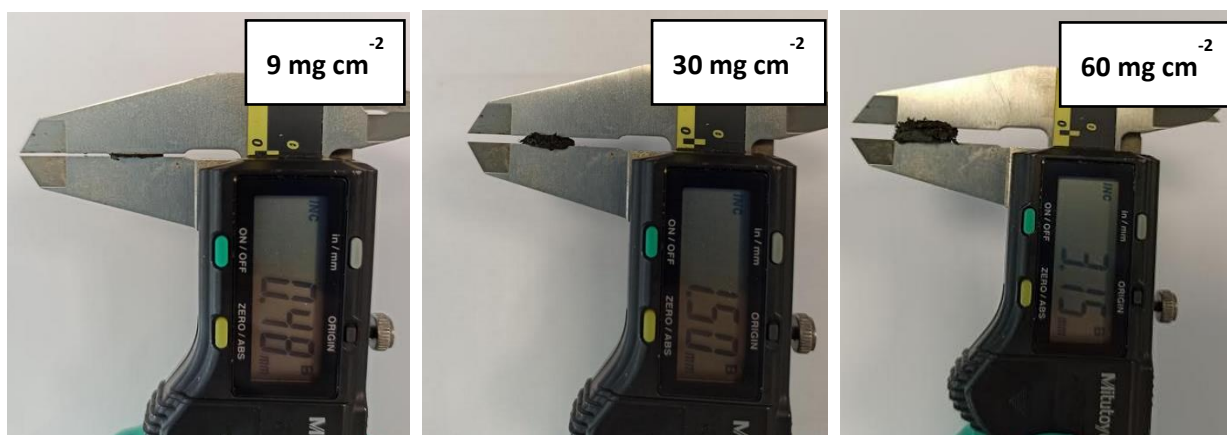


Figure S13. Thickness of the buckypaper electrodes determined by micrometer measurements. Thickness of electrodes were 0.48 mm, 1.50 mm and 3.15 mm for electrodes with mass loading of 9 mg cm^{-2} , 30 mg cm^{-2} and 60 mg cm^{-2} , respectively. The density of the electrode determined experimentally as (electrode mass/diameter x thickness) was 0.2 g cm^{-3} .

The porosity was calculated according to the following equation:

$$P = \frac{S - S_a}{S}$$

Where, S is the bulk density of the electrode (density of the material with same composition but without any porosity), taken from literature for similar conjugated microporous polymers as a range to $0.8\text{--}0.6 \text{ mg cm}^{-3}$. S_a is the apparent density defined as (electrode weight)/(electrode volume) and determined experimentally as 0.2 mg cm^{-3} . According to previous equation porosity of the reported electrodes were in the range of 65–75 %, in good agreement with literature.

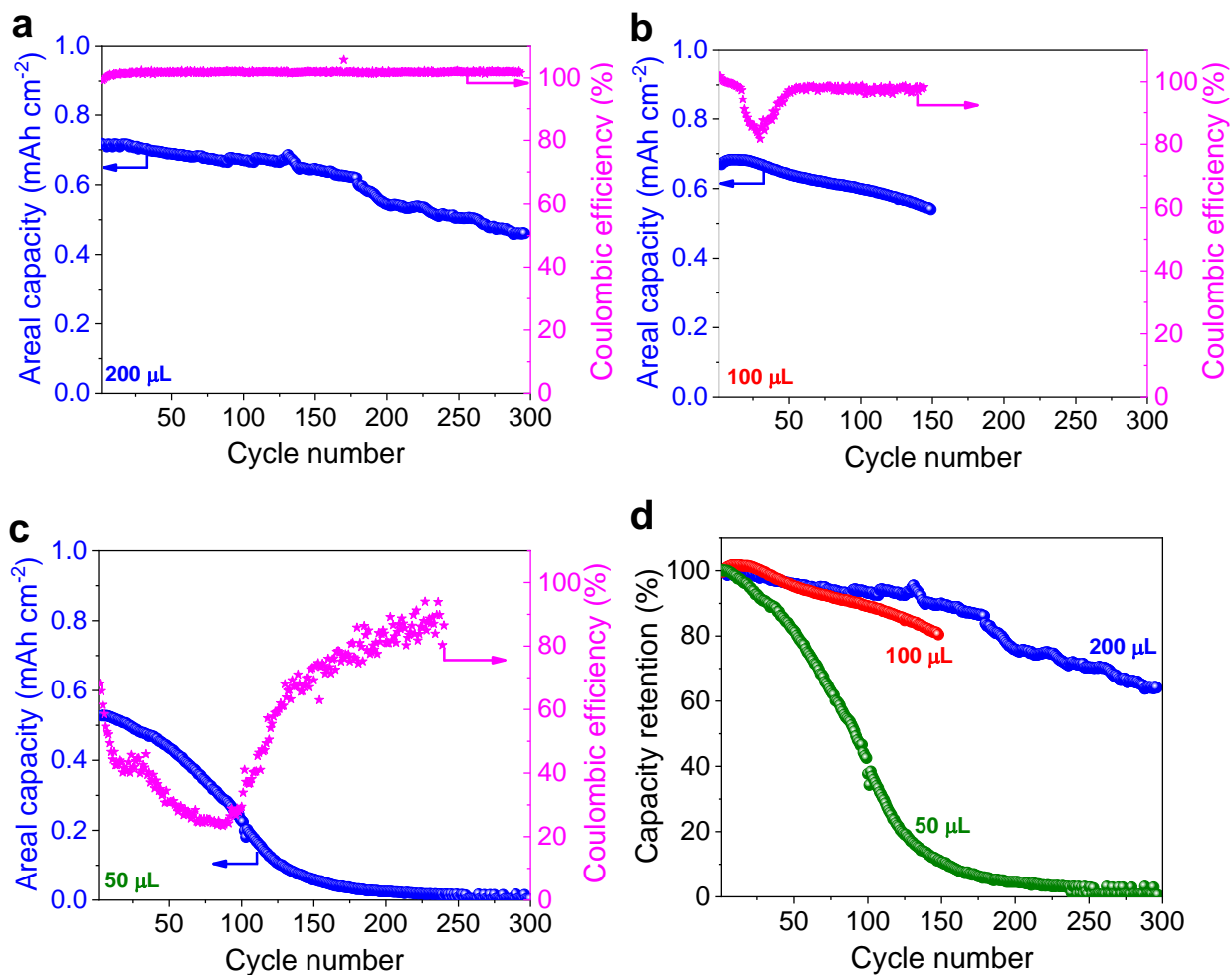


Figure S14. Cycle stability of IEP-11-S5R5@S10 buckypaper electrode (9.0 mg cm^{-2}) recorded at 1C (1.7 mA cm^{-2}) in Li-ion half-cell with different amount of electrolyte. (a – c) Areal capacity versus cycle number with 200 μL (a), 100 μL (b), and 50 μL (c) electrolyte. (d) Areal capacity retention plot.

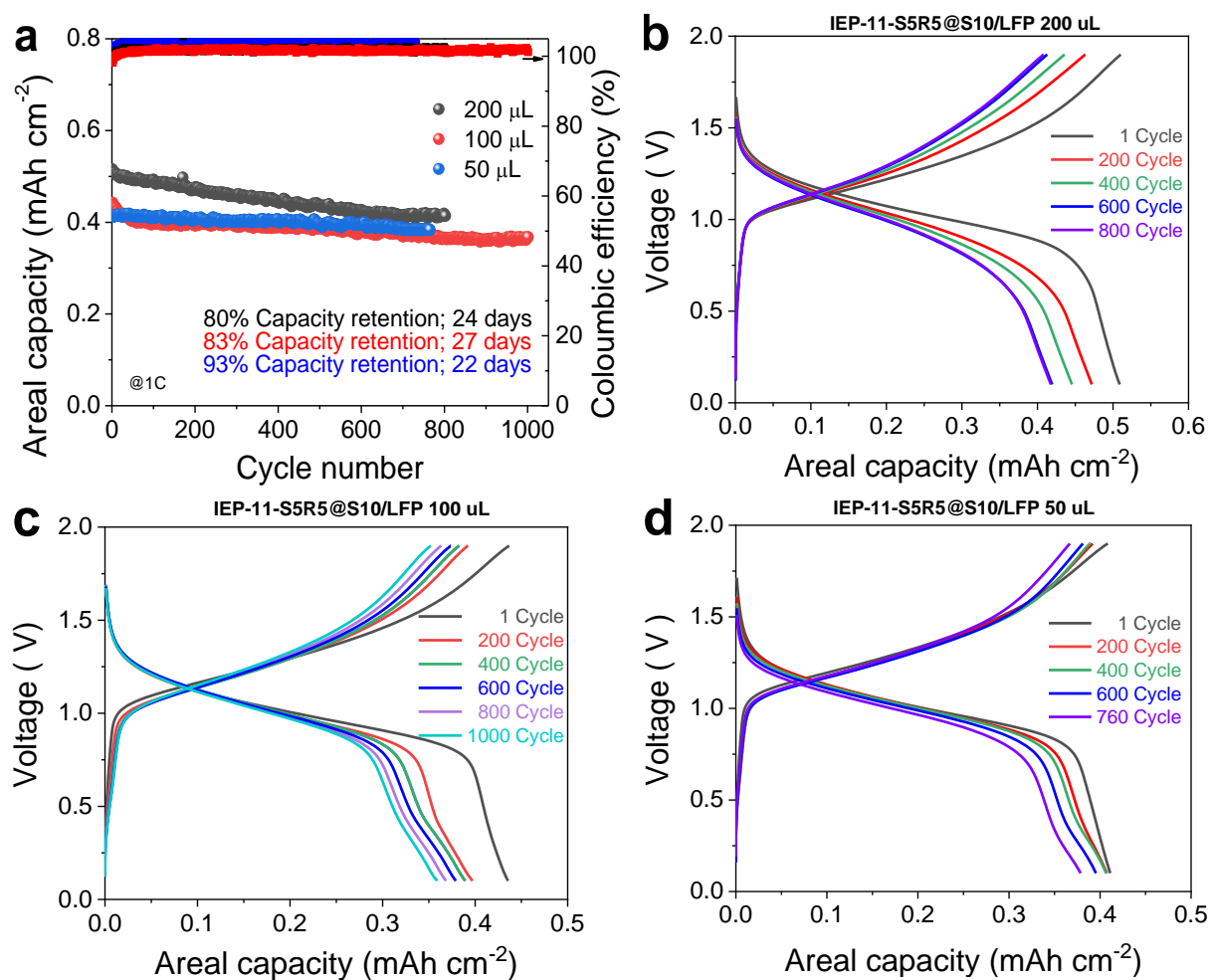


Figure S15. Cycle stability of IEP-11-S5R5@S10 buckypaper (9.0 mg cm⁻²) – custom LFP (3.5 mAh cm⁻²) full cell recorded at 1C (1.5 mA cm⁻²) with different amount of electrolyte. (a) Areal capacity versus cycle number with 200 μL, 100 μL, and 50 μL electrolyte. GCD profiles with 200 μL (b) 100 μL (c), and 50 μL (d) at different cycles.

Supplementary References

- (1) Yang, Z.; Tong, L.; Tabor, D. P.; Beh, E. S.; Goulet, M.-A.; De Porcellinis, D.; Aspuru-Guzik, A.; Gordon, R. G.; Aziz, M. J. Alkaline Benzoquinone Aqueous Flow Battery for Large-Scale Storage of Electrical Energy. *Adv. Energy Mater.* **2018**, 8 (8), 1702056. <https://doi.org/10.1002/aenm.201702056>.
- (2) Patry, G.; Romagny, A.; Martinet, S.; Froelich, D. Cost Modeling of Lithium-Ion Battery Cells for Automotive Applications. *Energy Sci. Eng.* **2015**, 3 (1), 71–82. <https://doi.org/10.1002/ese3.47>.
- (3) Molina, A.; Patil, N.; Ventosa, E.; Liras, M.; Palma, J.; Marcilla, R. New Anthraquinone-Based Conjugated Microporous Polymer Cathode with Ultrahigh Specific Surface Area for High-Performance Lithium-Ion Batteries. *Adv. Funct. Mater.* **2020**, 30 (6), 1908074. <https://doi.org/10.1002/adfm.201908074>.
- (4) Song, Z.; Xu, T.; Gordin, M. L.; Jiang, Y.-B.; Bae, I.-T.; Xiao, Q.; Zhan, H.; Liu, J.; Wang, D. Polymer–Graphene Nanocomposites as Ultrafast-Charge and -Discharge Cathodes for Rechargeable Lithium Batteries. *Nano Lett.* **2012**, 12 (5), 2205–2211. <https://doi.org/10.1021/nl2039666>.
- (5) Song, Z.; Qian, Y.; Gordin, M. L.; Tang, D.; Xu, T.; Otani, M.; Zhan, H.; Zhou, H.; Wang, D. Polyanthraquinone as a Reliable Organic Electrode for Stable and Fast Lithium Storage. *Angew. Chemie Int. Ed.* **2015**, 54 (47), 13947–13951. <https://doi.org/10.1002/anie.201506673>.
- (6) Suguro, M.; Iwasa, S.; Nakahara, K. Fabrication of a Practical and Polymer-Rich Organic Radical Polymer Electrode and Its Rate Dependence. *Macromol. Rapid Commun.* **2008**, 29 (20), 1635–1639. <https://doi.org/10.1002/marc.200800406>.
- (7) Wu, H.; Meng, Q.; Yang, Q.; Zhang, M.; Lu, K.; Wei, Z. Large-Area Polyimide/SWCNT Nanocable Cathode for Flexible Lithium-Ion Batteries. *Adv. Mater.* **2015**, 27 (41), 6504–6510. <https://doi.org/10.1002/adma.201502241>.
- (8) Wang, S.; Wang, Q.; Shao, P.; Han, Y.; Gao, X.; Ma, L.; Yuan, S.; Ma, X.; Zhou, J.; Feng, X.; Wang, B. Exfoliation of Covalent Organic Frameworks into Few-Layer Redox-Active Nanosheets as Cathode Materials for Lithium-Ion Batteries. *J. Am. Chem. Soc.* **2017**, 139 (12), 4258–4261. <https://doi.org/10.1021/jacs.7b02648>.
- (9) Wang, G.; Chandrasekhar, N.; Biswal, B. P.; Becker, D.; Paasch, S.; Brunner, E.; Addicoat, M.; Yu, M.; Berger, R.; Feng, X. A Crystalline, 2D Polyarylimide Cathode for Ultrastable and Ultrafast Li Storage. *Adv. Mater.* **2019**, 1901478, 1–6. <https://doi.org/10.1002/adma.201901478>.
- (10) Xu, F.; Jin, S.; Zhong, H.; Wu, D.; Yang, X.; Chen, X.; Wei, H.; Fu, R.; Jiang, D. Electrochemically Active, Crystalline, Mesoporous Covalent Organic Frameworks on Carbon Nanotubes for Synergistic Lithium-Ion Battery Energy Storage. *Sci. Rep.* **2015**, 5 (1), 8225. <https://doi.org/10.1038/srep08225>.
- (11) David, L.; Feldman, A.; Mansfield, E.; Lehman, J.; Singh, G. Evaluating the Thermal Damage Resistance of Graphene/Carbon Nanotube Hybrid Composite Coatings. *Sci. Rep.* **2015**, 4 (1), 4311. <https://doi.org/10.1038/srep04311>.
- (12) López-Lorente, A. I.; Simonet, B. M.; Valcárcel, M. Raman Spectroscopic Characterization of Single Walled Carbon Nanotubes: Influence of the Sample Aggregation State. *Analyst* **2014**, 139 (1), 290–298. <https://doi.org/10.1039/C3AN00642E>.